Effects of supercritical CO2 on micropores in bituminous and anthracite coal

Effects of Supercritical CO_2 on Micropores in Bituminous and Anthracite Coal

Shiqi Liu[a], Shuxun Sang[b,*], Jingsheng Ma[c], Tian Wang[b], Yi Du[b], Huihuang Fang[b]

The first two authors contributed equally to this work.

[a] *The Key Laboratory of Coal-based CO_2 Capture and Geological Storage, Jiangsu Province, Low Carbon Energy Institute, China University of Mining and Technology, Xuzhou 221116, China*

[b] *Key Laboratory of Coalbed Methane Resources and Reservoir Formation Process, Ministry of Education, School of Mineral Resource and Geoscience, China University of Mining and Technology, Xuzhou 221116, China*

[c] *Institute of Petroleum Engineering, Heriot-Watt University, EH14 4AS, United Kingdom*

Abstract: The effects of supercritical CO_2 ($ScCO_2$) on coal micropores play a critical role in determining the CO_2 capacity of coalbeds. To investigate the effects of $ScCO_2$ on micropores in coals of different ranks under a range of temperature and pressure conditions, CO_2 sequestration processes are replicated using a $ScCO_2$ geochemical reactor. Four samples of coal of different ranks are exposed to $ScCO_2$ and water for 240 h at 62.5 °C and 15 MPa, and CO_2 adsorption tests, Fourier transform infrared spectroscopy, and X-ray diffraction are performed to determine the volume and pore size distribution of the micropores, the types and contents of the organic groups, and the aromatic crystallite structures of the coal samples before and after the $ScCO_2$-H_2O treatment. The influence of the chemical structure and the organic groups of the coal on the coal micropores is then studied. Micropores with widths <0.46 nm are mainly associated with the inter-layer spacing of the aromatic layers. Swelling caused by $ScCO_2$ detaches heterocycles and non-condensed polynuclear aromatics of high-volatile bituminous coal, resulting in slight increases in the volume of micropores with widths <0.46 nm. The falling off of cross-links with low bond energies caused by swelling and the formation of C_{Ar}-C_{Ar} cross-links between the aromatic layers caused by polyaddition reactions together cause a decrease in the volume of micropores with widths <0.46 nm in semi-anthracite and anthracite coal. Micropores with widths >0.46 nm are pores in the macromolecular structure of coal and are known as intermolecular pores, and their volumes are determined by the directional arrangement of aromatic crystallites and the aliphatic hydrocarbon chain length. The broken bonds caused by $ScCO_2$ in high-volatile bituminous coal form new aliphatic or aromatic compounds via addition and polyaddition reactions. These processes increase the directional arrangement of aromatic crystallites, resulting in a decrease in the volume of micropores with widths >0.46 nm. As the coal rank increases, the aliphatic hydrocarbon chain length gives priority to the macromolecular structure of coal after the $ScCO_2$ treatment, resulting in an

increase in the volume of micropores with widths >0.46 nm in semi-anthracite and anthracite coal.

Keywords: Pore volume; Specific surface area; Organic group; Aromatic crystallite; Swelling; Coal rank

1. Introduction

CO_2 capture and geological storage are effective approaches for reducing greenhouse gas emissions. Deep coal seams are important geological bodies where CO_2 can potentially be stored [1]. CO_2 geological storage-enhanced coalbed methane recovery (CO_2-ECBM) can be used to enhance coalbed methane (CBM) development and reduce CO_2 emissions by effectively displacing CH_4 using CO_2, and this approach has attracted considerable attention from many researchers [2,3]. At in situ reservoir temperatures and pressures corresponding to burial depths >800 m (e.g., *T*c=31.06 °C, *P*c=7.38 MPa), CO_2 is likely to be present in a supercritical state [4]. The effects of supercritical CO_2 ($ScCO_2$) on the pores and fractures found in coal may lead to changes in the permeability and adsorption capacity of coal [5-7].

In our previous paper published in *Fuel* in 2018 [12], the effects of $ScCO_2$ on mesopores (2-50 nm in width), macropores (>50 nm in width) and fractures in coal with different ranks and the connectivity of pores and fractures within coal were studied. These pores and fractures are affected by changes in the inorganic minerals in coal (e.g., calcite, dolomite, and magnesite) caused by the $ScCO_2$-H_2O system [12]. Moreover, $ScCO_2$ displays good diffusivity and dissolving capacity; thus, it can dissolve some of the organic groups found on the inner surfaces of the pores and fractures in coal during the migration process [13-15]. This dissolution changes the physical and chemical structure of the coal and has a great influence on the micropores and CO_2 storage capacity of coal. The interactions between $ScCO_2$ and coal organic groups are affected by temperature, pressure, pore and fracture widths, and coal rank, among other factors [13,16,17]. At low pressures (7-10 MPa), $ScCO_2$ can extract limited amounts of polar hydrocarbons and lipids, e.g., alkanes and polycyclic aromatic hydrocarbons of relatively low molecular weights, esters, ethers, lactones, and epoxy compounds [18]. The effects of $ScCO_2$ on polar functional groups are weak [4]. At high pressures (>10 MPa), $ScCO_2$ can extract some aliphatic hydrocarbons, hydroxyl groups and other oxygen-containing groups and causes changes in the macromolecular structure of the coal and the destruction of the microcrystalline structure [17,19-22].

The interactions between $ScCO_2$ and coal organic groups mainly affect micropores, which have widths <2 nm [9,12,23,24]. Coal micropores are the primary sites for CBM adsorption and CO_2 storage. The pore volume, specific surface area (SSA), and pore size distribution of coal micropores are of great significance for CO_2-ECBM [25,26]. In addition, $ScCO_2$ has been suggested to decrease the volume percent of micropores in lignite/brown

coal and increase the volume percent and SSA of micropores in bituminous coal and anthracite [27-30]. Other scientists have suggested that $ScCO_2$ can increase the volume percent and SSA of micropores in lignite/brown coal and bituminous coal [27-30], whereas others have suggested that $ScCO_2$ can only break sub-agents in coal structure units but are unable to break the spatial structures of coal formed by chemical cross-links [31,32]. Therefore, $ScCO_2$ can change the pore size distribution in coal slightly. The interactions between $ScCO_2$ and coal organic groups can loosen the surfaces of coal particles and lead to macromolecular rearrangements and obvious plastification within coal, and these processes can enhance the porosity, permeability, and adsorption capacity of coal [5,33,34]. In conclusion, the effects of $ScCO_2$ on coal porosity, permeability, and adsorption capacity have been generally recognized. However, the effects of $ScCO_2$ on micropores in coal with different ranks and their mechanisms are still controversial, which limits our understanding of the adsorption capacity of coal and the efficiency of CO_2 displacement of CH_4.

In this paper, an integrated approach that combines CO_2 adsorption tests, Fourier transform infrared spectroscopy (FTIR), and X-ray diffraction (XRD) is employed to describe the effects of $ScCO_2$ on the micropores, chemical structures, and organic groups of bituminous coal and anthracite coal at 62.5 °C and 15 MPa. The effects and mechanisms of the chemical structures and organic groups on micropores are further discussed. This study is a continuation of our previous work published in *Fuel* in 2018 [12], and it aims to provide a better understanding of how $ScCO_2$ affects the micropores in coal with different ranks. The results can guide estimates of the CO_2 storage capacity in coal and the optimization of CO_2-ECBM engineering studies.

2. Samples and Methodology

2.1. Samples

Four samples of coal of different ranks were collected in China. High-volatile bituminous coal was collected from the Yangzhuang Mine, low-volatile bituminous coal was collected from the Xinyuan Mine, semi-anthracite coal was collected from the Yuwu Mine, and anthracite coal was collected from the Sihe Mine. These samples are named Coal #1 to Coal #4 (Table 1). Coal #1 was collected from coal seam #9 in the Taiyuan Formation in the Bohaiwan Basin, and Coals #2-#4 were collected from coal seam #3 of the Shanxi Formation in the southern Qinshui Basin. The coal samples were systematically collected from the working faces of the coal mines. To prevent further oxidization, the coal samples were wrapped in absorbent paper, hermetically sealed in plastic bags and stored at 5 °C after the samples were collected. The key properties of the samples are shown in Table 1.

2.2. $ScCO_2$-H_2O treatment

$ScCO_2$-H_2O treatments were performed to replicate a burial depth of 1500 m. The temperature and pressure at this burial depth (62.5 ℃ and 15 MPa, respectively) were calculated from the temperature and depth of the sub-surface constant temperature zone, the average geothermal gradient, and the average pressure gradient at the sampling location. The coal samples chosen for the $ScCO_2$-H_2O treatment consisted of 200 g of coal particles sieved to a grain size range of 4-8 mm. The details of the high-pressure reactor, coal grain size, and experimental duration used in the $ScCO_2$-H_2O treatment can be found in our previous paper [12]. After the $ScCO_2$-H_2O treatment, the coal samples were vacuum dried at 50 ℃ for 24 h and then crushed and sieved to different grain sizes for the CO_2 adsorption test, FTIR spectroscopy, and XRD analysis.

Table 1 Properties of the coals used

Sample	Sampling location	*Ro, max*, %	Proximate, wt. %				Ultimate, wt. %			
			M_{ad}	A_{ad}	V_{daf}	FC_{ad}	O_{daf}	C_{daf}	H_{daf}	N_{daf}
#1	Yangzhuang Mine	0.72	2.29	5.49	38.72	57.91	7.99	83.28	5.27	1.22
#2	Xinyuan Mine	1.81	0.81	5.35	15.26	80.20	9.30	80.32	4.43	1.14
#3	Yuwu Mine	2.19	1.10	11.98	13.44	76.19	2.44	91.73	4.12	2.44
#4	Sihe Mine	3.33	1.48	13.12	6.32	81.39	2.98	93.45	2.15	1.00

Notes: *Ro, max*, the mean maximum reflectance values of vitrinite; wt. %, weight percent; M_{ad}, moisture; A_{ad}, ash yield; V_{daf}, volatile matter; FC_{ad}, fixed carbon; O_{daf}, oxygen; C_{ad}, carbon; H_{ad}, hydrogen; N_{ad}, nitrogen; ad, air-dried basis; and daf, dry ash-free basis.

2.3 CO_2 adsorption test

This study uses a pore structure classification system proposed by the International Union of Pure and Applied Chemistry (IUPAC). Under this system, pores are divided into micropores (<2 nm in width), mesopores (2-50 nm in width) and macropores (>50 nm in width) [35].

The volume of the micropores within the coal samples and the SSA of the coal samples is measured using the CO_2 adsorption method, which is performed with an Autosorb iQ2 instrument made by Quantachrome Instruments, USA. The measurement procedures followed ISO 15901-2:2006 and ISO 15901-3:2007. Coal samples with a 20- to 80-mesh particle size (0.20-0.85 mm) were used in the CO_2 adsorption experiments, and CO_2 was used as the adsorbate at an analysis bath temperature of 273.0 K (0 °C). CO_2 adsorption isotherms are obtained at a relative pressure (P/P_0) range of 4.9624×10^{-4} to 2.8697×10^{-2}. The CO_2 adsorption data acquired from the pulverized coal were interpreted using the Dubinin-Astakhov (D-A) model to estimate the micropore volume, the Dubinin-Radushkevich (D-R) model (Eq. 1; a special form of the D-A model obtained for n=2) to estimate the SSA and the density functional theory (DFT) analysis to estimate the pore size distribution in a range from 0.30 to 1.50 nm [36-39].

$$\frac{V}{V_0} = \exp\left[-\left(\frac{RT}{\beta E_0}\ln\frac{p_0}{p}\right)^n\right] \quad (1)$$

where, V is the adsorbed volume at relative pressure p_0/p, 10^{-3} m^3/kg; p_0 is the CO_2 saturated vapor pressure at 273.0 K, MPa (the CO_2 saturated vapor pressure at 273.0 K is taken to be 3.48 MPa); V_0 is the maximum volume of gas adsorbed, 10^{-3} m^3/kg; E_0 is the characteristic adsorption energy of the reference fluid, J/mol; β is the similarity factor, which is the ratio of the molar volume of CO_2 and the molar volume of the reference fluid; R is the universal gas constant, 8.314472 $cm^3 \cdot MPa \cdot mol^{-1} \cdot K^{-1}$; T is the equilibrium temperature of CO_2 adsorption, 273.0 K; and n is the structural heterogeneity parameter, which takes values of 2-6 (n=2 and n>2 indicate larger numbers of micropores with sizes of 1.8-2 nm and <2 nm in the coal, respectively).

2.4 Fourier transform infrared spectroscopy

FTIR was carried out with a VERTEX 80v Fourier transform infrared spectrometer made by Bruker, Germany. To obtain accurate infrared spectra, coal samples no larger than 200 mesh (76 μm) were used in the experiment and were vacuum-dried at 50 °C for 24 h. The coal samples were prepared by the KBr disc technique. Pulverized coal was evenly mixed with KBr in a proportion of 1:180 (the sum of the weights is 0.1 g). A KBr disc (0.1 g) was used as a blank background. The scanned area was 400-4000 cm^{-1} at a scanning resolution of 4 cm^{-1}. The coal samples were scanned 32 times.

Table 2 Semi-quantitative ratios extracted from the FTIR spectra. [11,40,41,42]

Semi-quantitative index	Index calculation	Band region, cm^{-1}
Relative abundance of aliphatic groups (I_1)	aliphatic CH_x stretching vibration/aromatic C=C ring stretching vibration	$I_{2800\text{-}3000}/I_{1600}$
Relative abundance of aromatic groups (I_2)	aromatic CH_x asymmetrical deformation vibration/aromatic C=C ring stretching vibration	$I_{1439\text{-}1460}/I_{1600}$
Degree of oxygen-containing groups (I_3)	(aromatic C-O stretching vibration + hydrogen bond stretching vibration)/aromatic C=C ring stretching vibration	$(I_{1000\text{-}1338} + I_{3200\text{-}3600})/I_{1600}$
Aliphatic chain length (I_4)	R_2CH_2 stretching vibration/RCH_3 stretching vibration (CH_2/CH_3 Ratio)	I_{2925}/I_{2950}
Aromaticity 2 (AR2)	aromatic CH out-of-plane deformation/aliphatic CH_x stretching vibration	$I_{700\text{-}900}/I_{2800\text{-}3000}$
Degree of aromatic ring condensation 2 (DOC2)	aromatic CH out-of-plane deformation/aromatic C=C ring stretching vibration	$I_{700\text{-}900}/ I_{1600}$

The types and ratios of the major organic groups of coal samples were acquired via a semi-quantitative analysis of the FTIR spectra. By comparing the absorption frequency attributes of the coal molecules with the coal molecular structure, the major organic groups of the coal and their regions within the FTIR spectra can be

132 determined. According to the selected regions of the FTIR spectra of the coal samples, polynomial fitting was
133 performed to determine the baseline correction, and overlapping peaks of the selected regions were separated via
134 curve fitting using the OMNIC software package. Band shapes with Gaussian functions were then applied. The
135 positions and number of the bands were preliminarily established via the second derivative of the spectrum. The
136 ratios of the major organic groups were then analysed semi-qualitatively by calculating the peak areas of the
137 organic groups based on the Lambert-Beer law.

138 Semi-quantitative indexes extracted from FTIR spectra were applied to characterize the chemical structure of
139 the coal. Six structural parameters extracted from FTIR spectra by curve fitting analysis were used in this study
140 (Table 2). The relatively intense and stable absorption peaks were selected, and the band area was used in this
141 work.

142 **2.5 X-ray diffraction**

143 The XRD experiments were conducted using the D8 Advance X-ray diffractometer made by Bruker, Germany.
144 The coal samples used for the XRD experiments had a particle size of <325 mesh (0.045 mm). The XRD
145 experiment employed copper Ka radiation (40 kV, 40 mA), and the scanning range extended from 2 to 80° and
146 included a step distance of 0.1° and a scanning speed of 8 s/step.

147 XRD has been utilized to determine the structural parameters of coals, such as the fraction of aromaticity (f_a),
148 the inter-layer spacing of the crystalline structure, and crystallite sizes [33,43,44]. The overlapping peak in the 2θ
149 region of 15-35° can be fitted to two Gaussian peaks at approximately 20 and 26° using the MDI Jade 6.0
150 software package, and these peaks represent the γ and 002 bands, respectively. In principle, the areas under the γ
151 and 002 peaks are believed to be equal to the number of aromatic carbon atoms (C_{ar}) and aliphatic carbon atoms
152 (C_{al}), respectively [33,43]. Therefore, the f_a of coal, the ratio of carbon atoms in aliphatic chains vs. aromatic rings,
153 can be defined as follows [33,43]:

154 $$f_a = \frac{C_{ar}}{C_{ar} + C_{al}} = \frac{A_{002}}{A_{002} + A_{\gamma}} \qquad (2)$$

155 where A_{002} and A_{γ} are the integrated areas under the 002 and γ peaks, respectively, and C_{al} and C_{ar} are the numbers
156 of aliphatic and aromatic carbon atoms per structural unit, respectively.

157 The inter-layer spacing of the aromatic layers (d_{002}) can be calculated from the peak position using Bragg's
158 equation [45]:

$$d_{002} = \frac{\lambda}{2\sin\theta_{002}} \quad (3)$$

where d_{002} is the inter-layer spacing of the aromatic layers, Å; λ is the wavelength of the incident X-ray (for copper Ka radiation, λ=1.54056 Å); and θ_{002} is the scattering angle or peak position of the 002 peak.

Reports have suggested that the crystallite size can also be approximately calculated from the width of the corresponding band at half maximum intensity using empirical expressions first derived by Scherrer [33,42-44]:

$$L_a = \frac{K_a\lambda}{B_a\cos\theta_{100}} \quad (4)$$

$$L_c = \frac{K_c\lambda}{B_c\cos\theta_{002}} \quad (5)$$

where L_a is the average width of the coal crystallites, Å; L_c is the average height of the coal crystallites, Å; K is a constant that depends on the reflection plane, and the value is 1.84 for the 100 peak and 0.89 for the 002 peak; B_a and B_c are the widths of the 100 and 002 peaks at the half maximum intensity, respectively; and θ_{100} is the scattering angle or peak position of the 100 peak.

The average number of the aromatic layers (N_c) can be estimated from d_{002} and L_c using the following equation [46]:

$$N_c = \frac{L_c}{d_{002}} \quad (6)$$

3. Results

3.1 Micropore analyses using CO_2 adsorption tests

3.1.1 Variations in micropore volume and the SSA

The volume of the micropores in the coal samples is 0.049-0.068 cm^3/g, the SSA is 146.708-304.682 m^2/g, and the average pore width is 0.627-0.501 nm (Table 3). As the coal rank increases, both the volume and the SSA of the micropores increase, and the increase in the micropore SSA (85.02-107.68 %) is much larger than the increase in the micropore volume (14.29-38.78 %). Conversely, the pore width decreases as the coal rank increases (Table 3). This result shows that coal with a higher rank has a more compact chemical structure with a smaller micropore width.

After the $ScCO_2$ treatment, the volume and SSA of the micropores in Coal #1 decreased (10.20 % and 48.95 %, respectively) while the average pore width was fixed (Table 3). The volume, SSA, and average pore width of the

micropores in Coals #2-#4 increased (Table 3). As the coal rank increases, the volume (12.50 %, 14.71 %, and 27.69 %, respectively) and SSA (109.48 %, 212.04 %, and 209.60 %, respectively) of the micropores in Coals #2-#4 increase (Table 3). Although the increase in micropore volume is lower than that of the SSA, their patterns of variation are highly consistent (Table 3).

Table 3 Micropore volume, SSA, and other pore structure parameters determined by CO_2 adsorption applied to the coal samples.

Sample		DR SSA, m^2/g	DA pore volume, ml/g	Average pore width, nm	Pore width of the peak, nm
#1	Untreated	146.708	0.049	0.627	0.524/0.627/0.751/0.822
	$ScCO_2$ treated	74.889	0.044	0.627	0.366/0.501/0.627/0.751/0.822
#2	Untreated	273.349	0.056	0.627	0.501/0.627/0.751/0.859
	$ScCO_2$ treated	572.620	0.063	0.673	0.573/0.718/0.822
#3	Untreated	271.446	0.068	0.501	0.319/0.501/0.600/0.786/0.859
	$ScCO_2$ treated	847.009	0.078	0.600	0.524/0.600/0.718/0.822
#4	Untreated	304.682	0.065	0.501	0.319/0.418/0.501/0.573/0.822
	$ScCO_2$ treated	943.288	0.083	0.524	0.524/0.600/0.822

3.1.2 Variations in pore size distribution

The coal samples show a pore size distribution that includes multiple peaks (generally 3-4) that occur at 0.50 nm (0.46-0.55 nm), 0.63 nm (0.55-0.69 nm), 0.75 nm (0.69-0.79 nm), and 0.82 (0.79-1.50 nm) (Table 3, Fig. 1). Coals #1 and #2 have 3 main peaks located at 0.50 nm, 0.63 nm, and 0.82 nm, and the peak located at 0.75 nm is smaller (Fig. 1a, b). Coals #3 and #4 display 2 main peaks located at 0.50 nm and 0.63 nm (Fig. 1c, d). As the coal rank increases, the peaks that occur at 0.75 nm and 0.82 nm tend to unite, and the peak located at 0.75 nm, which is seen in the results for Coal #4, disappears (Fig. 1). Meanwhile, Coal #4 displays 5 peaks. Compared with Coals #1-#3, Coal #4 does not display the peak located at 0.75 nm, whereas it displays 2 additional peaks located at 0.32 nm (0.30-0.36 nm) and 0.42 nm (0.38-0.46 nm) (Fig. 1d), indicating that micropores with widths <0.46 nm are more strongly developed in the anthracite coal samples. The peak located at 0.32 nm also appears in Coal #3 (Fig. 1c); however, the peak is very small and may have been caused by measurement uncertainty.

After the $ScCO_2$ treatment, the peak values of Coal #1 decreased while the morphology of the peaks changed slightly, indicating that $ScCO_2$ significantly decreased the micropore volume in the high-volatile bituminous coal and had little influence on the pore size distribution (Fig. 1a). Thus, the average pore width of Coal #1 does not change. After the $ScCO_2$ treatment, Coal #1 displays one additional small peak located at 0.36 nm (0.32-0.44 nm) (Fig. 1a), indicating that $ScCO_2$ increased the volume of micropores with widths <0.46 nm in Coal #1. The micropore volume under the peaks located at 0.75 nm and 0.82 nm in Coals #2-#4 increased slightly (Fig. 1b, c, d). The changes in micropore volume are mainly concentrated in the peaks with small pore widths (0.50 nm and 0.63

nm; Fig. 1b, c, d), resulting in an increase in the micropore SSA of Coals #2-#4 that is much larger than the micropore volume. With the increase in pore width under the peak located at 0.50 nm, the peak located at 0.50 nm merges with the peak located at 0.63 nm, thus forming a new peak located at 0.57 nm (0.48-0.69 nm) in Coals #2-#4. This process causes a decrease in the volume of micropores with widths of 0.48-0.57 nm and an increase in the volume of micropores with widths >0.57 nm (Fig. 1b, c, d). In addition, micropores with widths <0.46 nm almost disappear in the semi-anthracite and anthracite coal, and the decrease in micropore volume is more obvious in the anthracite due to the greater abundance of micropores with widths <0.46 nm (Fig. 1c, d).

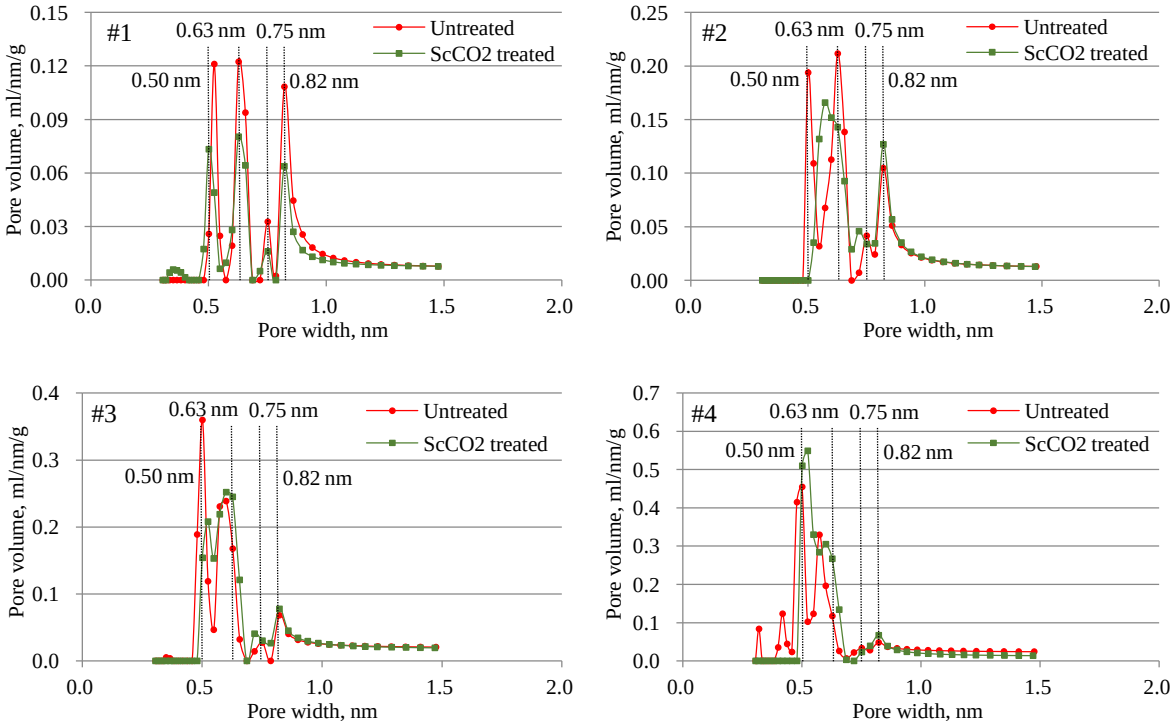

Fig. 1. Pore size distribution determined via CO_2 adsorption for the coal samples

The effects of the pore size distribution on the micropore volume are more significant in the cumulative pore volume results. After the $ScCO_2$ treatment, the change in the cumulative pore volume occurs in stages. Coal #1 displays one additional small peak located at 0.36 nm, resulting in a slight increase in the volume of micropores with widths <0.46 nm. With the decrease in micropore volume under the peaks located at 0.50 nm, 0.63 nm, 0.75 nm, and 0.82 nm, the volume of micropores with widths >0.63 nm in Coal #1 is smaller than that of raw coal (Fig. 2a). In Coal #2, the volume of the micropores with widths <0.46 nm is basically unchanged, whereas in Coals #3 and #4, the micropore volume decreases due to the disappearance of the peaks that occur at 0.32 nm and 0.42 nm (Fig. 2b, c, d). With the increase in micropore volume under the peak located at 0.50 nm, the volume of micropores with widths >0.46 nm gradually decreases after the $ScCO_2$ treatment. The micropore volume after the

226 $ScCO_2$ treatment exceeds the micropore volume in the raw coal when the pore width is >0.79 nm (low-volatile
227 bituminous coal), >0.63 nm (semi-anthracite coal), and >0.57 nm (anthracite; Fig. 2b, c, d). As the coal rank
228 increases, the volume of micropores with widths >0.46 nm increases (Fig. 2b, c, d). The increase in the cumulative
229 pore volume of the micropores with widths >0.79 nm in Coals #2-#4 is small (Fig. 2) because of the weak changes
230 in the volume of micropores with widths >0.79 nm after the $ScCO_2$ treatment (Fig. 1).

231

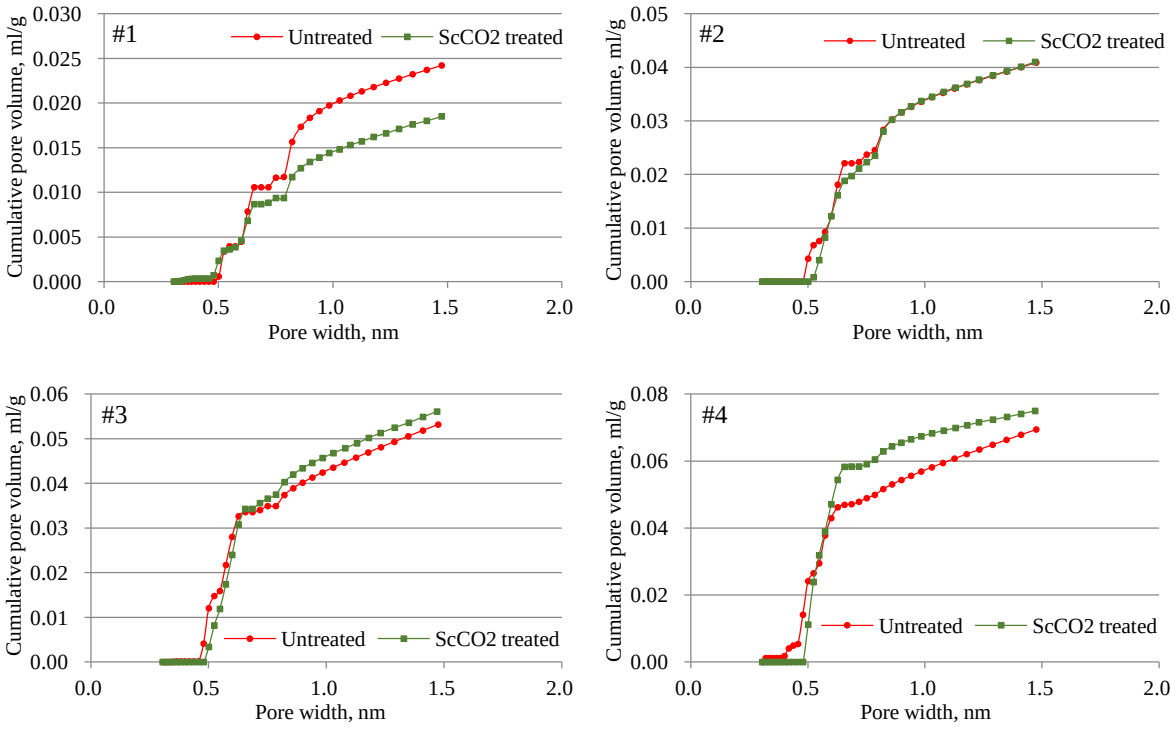

232

233 **Fig. 2.** Cumulative pore volume of CO_2 adsorption for the coal samples

234 **3.2 Variations in crystallite structure characteristics of the coal samples**

235 Two broadened diffraction peaks are observed in the XRD spectra of the coal samples, and the diffraction
236 angles are 20-30° and 40-50° (Fig. 3). These 2 diffraction peaks are in accordance with the 002 and 100 peaks of
237 natural graphite, which display diffraction angles of 26.6° and 43.4°, respectively. The 002 peak is more obvious
238 than the 100 peak in the XRD spectra of the coal samples (Fig. 3) and overlaps with the γ peak located to the left
239 of the 002 peak, which produces an asymmetrical distribution. As the coal rank increases, the γ peak intensity
240 decreases as the aliphatic structures decrease, which results in a more regular XRD spectra (Fig. 3). After the
241 $ScCO_2$ treatment, the XRD spectra of Coals #2-#4 show no marked changes, especially the position and shape of
242 the 002 peak and the 100 peak. This result indicates that Coals #2-#4 have similar crystallite structures before and
243 after the $ScCO_2$ treatment. The XRD spectra of Coal #1 are significantly affected by minerals that produce several
244 sharp diffraction peaks in the XRD spectra of Coal #1, and some minerals are still present after the $ScCO_2$

treatment (Fig. 3).

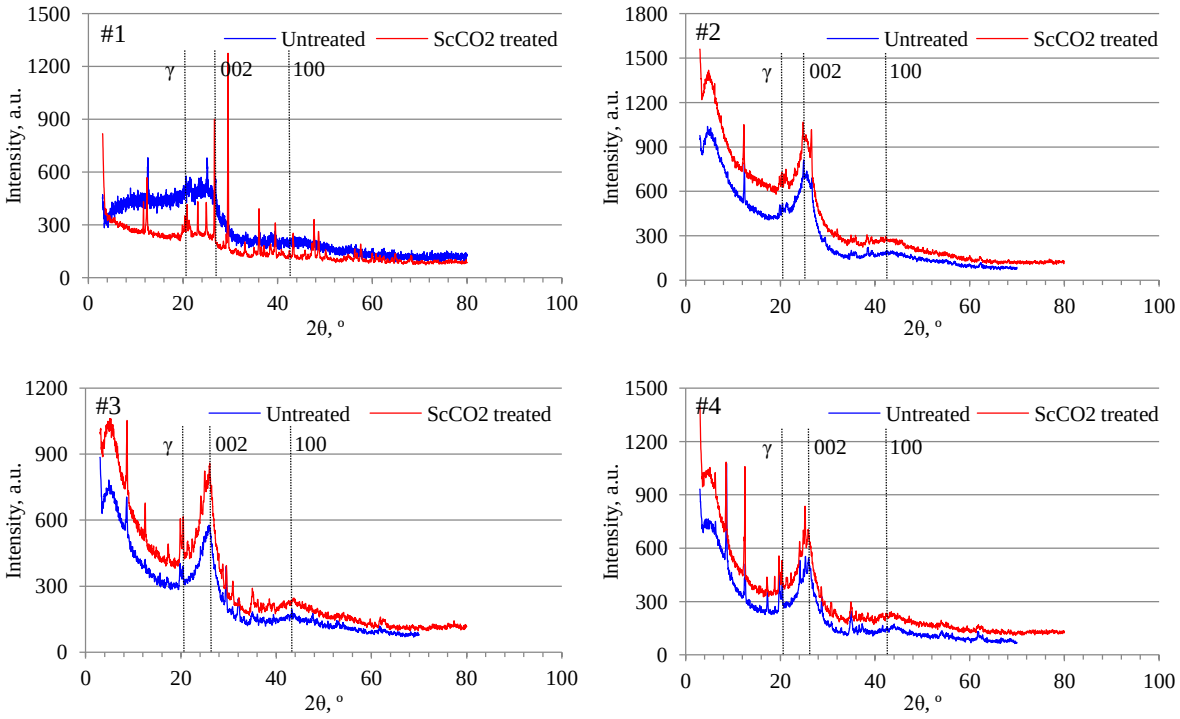

Fig. 3. XRD spectra of the coal samples

As the coal rank increases, the degree of aromatic ring condensation increases while the contents of bridge bonds, side chains, and oxygen-containing groups decrease, resulting in an increase in f_a (41.69-79.00; Table 4). Furthermore, the crystallite structures of the coal samples tend to transform to graphitic crystalline structures. Therefore, the L_a (25.78-26.63 Å) and L_c (11.06-11.76 Å) values of the coal samples increase while the d_{002} values (3.55-3.45 Å) decrease, causing increases in N_c (3.12-3.41; Table 4).

Table 4 Structural parameters extracted from the XRD spectra.

	Sample	θ_{002}, °	θ_{100}, °	d_{002}, Å	L_c, Å	L_a, Å	N_c	f_a
#1	Untreated	12.55	21.28	3.55	11.06	25.78	3.12	41.69
	$ScCO_2$ treated	12.46	21.22	3.57	11.06	25.13	3.10	55.62
#2	Untreated	12.66	21.74	3.51	11.07	26.08	3.15	63.69
	$ScCO_2$ treated	12.62	21.16	3.53	10.98	24.92	3.11	67.52
#3	Untreated	12.95	21.64	3.44	11.17	26.41	3.25	69.27
	$ScCO_2$ treated	13.02	21.53	3.42	10.91	26.73	3.19	65.47
#4	Untreated	12.91	21.67	3.45	11.76	26.63	3.41	79.00
	$ScCO_2$ treated	13.02	21.64	3.42	10.99	26.75	3.21	76.61

After the $ScCO_2$ treatment, the d_{002} values of Coal #1 and #2 increase slightly, while those of Coals #3 and #4 decrease slightly (Table 4). The L_c values of the coal samples tend to decrease, and these decreases become more pronounced as the coal rank increases (0, 0.81 %, 2.33 %, and 6.55 %, respectively; Table 4). This observation explains why the decrease in the N_c values of the semi-anthracite and anthracite coals is larger than that of the

bituminous coal (0.64 %, 1.27 %, 1.85 %, and 5.87 %, respectively; Table 4). Compared with the results for d_{002}, the L_a values of Coal #1 and #2 decrease slightly, while those of Coals #3 and #4 increase slightly (Table 4). In addition, the f_a values of Coal #1 increase, while those of Coal #2 increase slightly, and those of Coals #3 and #4 decrease slightly (Table 4), indicating that after the $ScCO_2$ treatment, the degree of aromatic ring condensation of bituminous coal tends to increase, while that of semi-anthracite and anthracite tends to decrease.

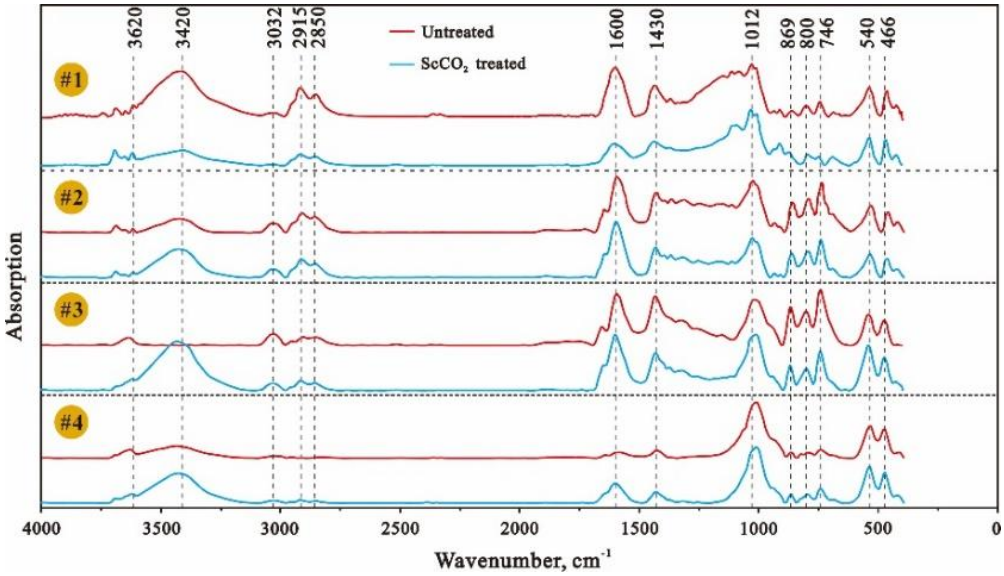

Fig. 4. FTIR spectra of the coal samples

3.3 FTIR characteristics of the coal samples

The FTIR spectra of the coal samples mainly contain the absorbance peaks of aromatic nuclei (1600 cm^{-1}), aromatic groups (700-900 cm^{-1}), oxygen-containing groups (1000-1800 cm^{-1}; exceptions include the absorbance peaks of aromatic nuclei at 1600 cm^{-1} and the deformation vibration absorption peaks of CH_3- and CH_2- at 1439-1460 cm^{-1}), aliphatic hydrocarbons (2800-3000 cm^{-1}), and hydroxyl groups (3000-3600 cm^{-1}; Fig. 4). Absorption peaks of minerals are also observed in the FTIR spectra, and these peaks are mainly the absorption peaks of quartz (466 cm^{-1}), clay minerals (540 cm^{-1}), and silicate minerals and kaolinite (3600-3700 cm^{-1}; e.g., hydromica at 3620 cm^{-1} and hydroxyl in kaolinite at 3690 cm^{-1}; Fig. 4). The coal samples yield FTIR spectra with similar shapes but significantly different absorbance peak intensities, indicating that the coal samples have similar types of organic groups and differ substantially in the contents of these organic groups. After the $ScCO_2$ treatment, the absorbance peak intensities of hydroxyl groups, aromatic nuclei, aromatic groups, oxygen-containing groups, and aliphatic hydrocarbons in Coal #1 decrease (Fig. 4). The absorbance peak intensities of hydroxyl groups and oxygen-containing groups in Coals #2-#4 increase, while that of the aromatic nucleus, aromatic groups, and aliphatic hydrocarbon decrease. As the coal rank increases, these decreases become more pronounced (Fig. 4).

Table 5 Aromatic C-H out-of-plane deformation bands extracted from the FTIR spectra.

Sample	Untreated				$ScCO_2$ treated			
	Peak index	Position, cm^{-1}	Area percentage, %	Assignment	Peak index	Position, cm^{-1}	Area percentage, %	Assignment
#1	1	725.30	6.45	$(CH_3)_n$ (n≥)4	1	749.47	18.42	4H
	2	746.78	33.18	4H	2	777.58	16.40	3H
	3	791.82	17.97	3H	3	797.85	17.18	3H
	4	808.99	21.31	2H	4	817.68	3.81	2H
	5	863.56	21.08	1H	5	848.12	7.49	2H
	6				6	875.06	36.71	1H
#2	1	715.73	8.37	$(CH_3)_n$ (n≥)4	1	720.72	6.70	$(CH_3)_n$ (n≥4)
	2	743.58	33.89	4H	2	746.49	32.84	4H
	3	796.72	30.74	3H	3	799.73	33.05	3H
	4	838.96	9.91	2H	4	836.09	6.25	2H
	5	867.02	17.10	1H	5	867.84	21.17	1H
#3	1	717.49	13.11	$(CH_3)_n$ (n≥)4	1	721.57	13.18	$(CH_3)_n$ (n≥4)
	2	743.64	32.33	4H	2	745.28	34.31	4H
	3	784.01	6.93	3H	3	787.98	8.48	3H
	4	800.63	11.33	3H	4	804.84	13.52	3H
	5	824.80	15.47	2H	5	826.87	8.42	2H
	6	866.80	20.84	1H	6	867.97	22.10	1H
#4	1	723.10	13.72	$(CH_3)_n$ (n≥4)	1	714.52	6.14	$(CH_3)_n$ (n≥4)
	2	748.26	33.43	4H	2	731.03	9.15	4H
	3	782.25	7.54	3H	3	742.94	12.41	4H
	4	798.88	13.84	3H	4	754.32	18.57	4H
	5	816.76	7.46	2H	5	784.30	7.71	3H
	6	830.75	5.71	2H	6	795.95	9.26	3H
	7	869.74	18.31	1H	7	811.08	14.26	2H
	8				8	831.06	4.46	2H
	9				9	869.80	18.04	1H

Note: $(CH_3)_n$ (n≥4) denotes single substitution.

3.3.1 Variations in aromatic structures

The coal samples are dominated by 4H (735-750 cm^{-1}) and 3H (750-810 cm^{-1}), followed by 1H (860-900 cm^{-1}), which displays the lowest contents of $(CH_3)_n$ (n≥4) (710-725 cm^{-1}), and 2H (810-860 cm^{-1}; Table 5). As the coal rank increases, the 2H contents generally decrease and the 4H and 1H contents change slightly (Table 5). Coals #3 and #4 have larger contents of $(CH_3)_n$ (n≥4) (13.11 % and 13.72 %, respectively), and the contents show a rising trend as the coal rank increases, indicating that high-rank coals have low contents of substituents in the aromatic

groups (Table 5). Overall, Coal #1 has the smallest content of aromatic groups (4.58 %) and lowest I_2 values (0.38) due to the large content of oxygen-containing groups (33.22 %) and hydroxyl structures (33.96 %; Table 6, 7). As the coal rank increases, the aromatic group contents and I_2 values of coal samples increase significantly (Table 6, 7).

Table 6 Variations in the percentage of the absorption peak area extracted from the FTIR spectra, %.

Assignment	Position, cm^{-1}	Untreated				$ScCO_2$ treated			
		#1	#2	#3	#4	#1	#2	#3	#4
Aromatic CH out-of-plane deformation	700-900	4.59	16.60	26.00	9.29	5.87	14.45	10.87	7.51
Aromatic C-O stretching vibration	1000-1800	33.22	38.67	27.44	44.81	46.27	27.62	24.12	25.62
Aliphatic CH_x stretching vibration	2800-3000	8.55	7.18	4.42	0.93	5.74	7.58	3.10	1.93
Hydrogen bond stretching vibration	3000-3600	33.96	8.56	0.58	32.60	19.61	23.52	36.19	48.91
Aromatic C=C ring stretching vibration	1600	11.59	15.03	20.34	5.69	9.41	14.74	15.58	9.91
Aromatic CH_x deformation vibration	1370-1480	7.62	12.05	18.00	5.35	12.91	10.08	8.81	4.96
Aromatic CH stretching vibration	3000-3100	0.46	1.90	3.22	1.35	0.19	2.01	1.33	1.16

Table 7 Structural parameters extracted from the FTIR spectra.

Sample		I_1	I_2	I_3	I_4	AR2	DOC2
#1	Untreated	0.74	0.38	5.68	2.78	0.54	0.40
	$ScCO_2$ treated	0.61	0.62	6.76	2.83	1.02	0.62
#2	Untreated	0.48	0.45	2.95	2.40	2.31	1.10
	$ScCO_2$ treated	0.51	0.38	3.26	2.59	1.91	0.98
#3	Untreated	0.22	0.48	1.16	3.97	5.89	1.28
	$ScCO_2$ treated	0.20	0.34	3.72	5.59	3.50	0.70
#4	Untreated	0.16	0.46	13.34	0.59	10.01	1.63
	$ScCO_2$ treated	0.19	0.29	7.30	2.80	3.89	0.76

After the $ScCO_2$ treatment, the aromatic group contents (1.28 %) and I_2 values of Coal #1 increase slightly, whereas those of Coals #2-#4 show a decreasing trend (Table 6, 7). The content of $(CH_3)_n$ ($n \geq 4$) in Coal #3 is basically unchanged (increase 0.48 %), whereas that of Coal #1, #2 and #4 is significantly decreased (100.00 %, 19.97 %, and 55.23 %, respectively; Table 5). As the coal rank increases, the 4H contents vary from a significant decrease for Coal #1 (44.50 %) and a slight decrease for Coal #2 (3.12 %) to a slight increase for Coal #3 (6.12 %) and a significant increase for Coal #4 (20.03 %; Table 5). As the coal rank increases, the 3H contents increase for Coals #1-#3 (86.80 %, 7.53 %, and 20.52, respectively) and significantly decrease for Coal #4 (20.60 %; Table 5). Coal #4 displays a significant increase in the 2H content (42.20 %) and a slight decrease in the 1H content (1.46 %). Conversely, Coals #1-#3 display a strong decrease in the 2H contents and an increase in the 1H contents (Table 5). As the coal rank increases, the increases in 1H contents (74.14 %, 23.81 %, and 6.05 %, respectively) become less pronounced. (Table 5). In general, the coal samples display predominantly substitution reactions

under $ScCO_2$ treatment, which causes a considerable increase in the substituents. As the coal rank increases, the bond dissociation reactions gradually increase, producing decreases in the aromatic group contents and I_2 values of Coals #2-#4 (Table 6, 7).

3.3.2 Variations in $ScCO_2$ on oxygen-containing structures

As the coal rank increases, the oxygen-containing group content and I_3 values decrease rapidly, and Coal #4 presents the largest contents of oxygen-containing groups and values of I_3 (Table 6, 7). The oxygen-containing groups in the coal samples are predominantly alkyl ethers (1030-1040 cm^{-1}), 2°C-O secondary (sec.) alcohols (1100-1125 cm^{-1}), 2°C-O phenols, ethers (1150-1250 cm^{-1}), and 2°C-O in aryl ethers (1260-1351 cm^{-1}), and they present small contents of carboxyl (quinone) C=O (1650-1690 cm^{-1}), carboxyl (ketone) C=O (1690-1760 cm^{-1}), and aryl esters (1760-1800 cm^{-1}; Table 8). Coals #1 and #2 are dominated by 2°C-O phenols and ethers, followed by 2°C-O sec. alcohols, and they present the lowest contents of 2°C-O in aryl ethers and alkyl ethers (Table 8). Coal #3 is dominated by 2°C-O in aryl ethers, followed by 2°C-O phenols, ethers and alkyl ethers, and it presents low contents of 2°C-O sec. alcohols (Table 8). Finally, Coal #4 is dominated by alkyl ethers and 2°C-O sec. alcohols, and it presents small contents of other oxygen-containing groups (Table 8).

Table 8 Oxygen-containing functional groups and aromatic nuclei extracted from the FTIR spectra.

Sample	Untreated				$ScCO_2$ treated			
	Peak index	Position, cm^{-1}	Area percentage, %	Assignment	Peak index	Position, cm^{-1}	Area percentage, %	Assignment
#1	1	1043.82	13.11	alkyl ethers	1	1036.69	22.42	alkyl ethers
	2	1083.30	16.27	2°C-O sec. alcohols	2	1081.43	15.97	2°C-O sec. alcohols
	3	1114.53	8.46	2°C-O sec. alcohols	3	1117.44	15.32	2°C-O sec. alcohols
	4	1143.58	12.33	2°C-O phenols, ethers	4	1166.06	14.68	2°C-O phenols, ethers
	5	1184.64	20.01	2°C-O phenols, ethers	5	1217.10	8.91	2°C-O phenols, ethers
	6	1230.29	8.33	2°C-O phenols, ethers	6	1260.65	7.48	2°C-O in aryl ethers
	7	1267.26	8.16	2°C-O in aryl ethers	7	1296.80	4.74	2°C-O in aryl ethers
	8	1312.79	5.97	2°C-O in aryl ethers	8	1330.02	5.61	2°C-O in aryl ethers
	9	1345.38	3.24	2°C-O in aryl ethers	9	1642.62	3.67	carboxyl (quinone) C=O
	10	1646.77	2.91	carboxyl (quinone) C=O	10	1690.04	0.98	carboxyl (quinone) C=O
	11	1700.16	0.49	carboxyl (ketone) C=O	11	1734.69	0.21	carboxyl (ketone) C=O
	12	1733.68	0.62	carboxyl (ketone) C=O	12	1772.60	0.02	aryl esters
	13	1773.37	0.11	aryl esters	13			
#2	1	1035.02	13.01	alkyl ethers	1	1037.78	14.21	alkyl ethers
	2	1075.47	13.02	2°C-O sec. alcohols	2	1074.14	12.80	2°C-O sec. alcohols
	3	1118.23	7.25	2°C-O sec. alcohols	3	1116.28	7.12	2°C-O sec. alcohols
	4	1151.93	8.71	2°C-O phenols, ethers	4	1150.97	7.84	2°C-O phenols, ethers

	5	1185.90	8.59	2°C-O phenols, ethers	5	1183.53	7.21	2°C-O phenols, ethers
	6	1222.18	8.71	2°C-O phenols, ethers	6	1223.39	10.04	2°C-O phenols, ethers
	7	1255.00	7.26	2°C-O in aryl ethers	7	1259.81	7.04	2°C-O in aryl ethers
	8	1292.93	11.03	2°C-O in aryl ethers	8	1296.94	8.34	2°C-O in aryl ethers
	9	1335.68	14.73	2°C-O in aryl ethers	9	1333.51	14.25	2°C-O in aryl ethers
	10	1653.86	5.22	carboxyl (quinone) C=O	10	1652.53	10.23	carboxyl (quinone) C=O
	11	1723.83	1.19	carboxyl (ketone) C=O	11	1710.04	0.28	carboxyl (ketone) C=O
	12	1754.96	0.57	carboxyl (ketone) C=O	12	1730.71	0.44	carboxyl (ketone) C=O
	13	1784.09	0.70	aryl esters	13	1769.50	0.20	aryl esters
	1	1035.64	16.77	alkyl ethers	1	1034.22	22.01	alkyl ethers
	2	1067.51	8.17	Si-O	2	1070.22	14.13	2°C-O sec. alcohols
	3	1094.28	2.67	2°C-O sec. alcohols	3	1118.12	9.16	2°C-O sec. alcohols
	4	1132.08	3.18	2°C-O sec. alcohols	4	1151.91	2.89	2°C-O phenols, ethers
	5	1150.11	3.79	2°C-O phenols, ethers	5	1180.88	6.82	2°C-O phenols, ethers
	6	1205.02	14.10	2°C-O phenols, ethers	6	1221.79	5.83	2°C-O phenols, ethers
#3	7	1256.81	12.00	2°C-O in aryl ethers	7	1259.94	8.08	2°C-O in aryl ethers
	8	1295.98	8.13	2°C-O in aryl ethers	8	1307.75	11.70	2°C-O in aryl ethers
	9	1325.03	14.90	2°C-O in aryl ethers	9	1346.19	9.90	2°C-O in aryl ethers
	10	1655.81	9.66	carboxyl (quinone) C=O	10	1654.12	9.01	carboxyl (quinone) C=O
	11	1718.51	0.67	carboxyl (ketone) C=O	11	1702.86	0.10	carboxyl (ketone) C=O
	12	1747.02	2.63	carboxyl (ketone) C=O	12	1741.55	0.27	carboxyl (ketone) C=O
	13	1797.15	3.32	aryl esters	13	1770.47	0.10	aryl esters
	1	1032.60	47.70	alkyl ethers	1	1034.02	47.19	alkyl ethers
	2	1072.70	21.83	2°C-O sec. alcohols	2	1071.41	26.87	2°C-O sec. alcohols
	3	1110.92	18.57	2°C-O sec. alcohols	3	1112.99	11.95	2°C-O sec. alcohols
	4	1175.38	2.57	2°C-O phenols, ethers	4	1170.97	1.66	2°C-O phenols, ethers
	5	1215.39	2.71	2°C-O phenols, ethers	5	1255.41	0.76	2°C-O in aryl ethers
#4	6	1255.46	1.55	2°C-O in aryl ethers	6	1322.40	3.08	2°C-O in aryl ethers
	7	1298.02	1.63	2°C-O in aryl ethers	7	1653.03	7.51	carboxyl (quinone) C=O
	8	1646.40	2.25	carboxyl (quinone) C=O	8	1702.54	0.22	carboxyl (ketone) C=O
	9	1712.23	0.27	carboxyl (ketone) C=O	9	1740.96	0.54	carboxyl (ketone) C=O
	10	1743.88	0.52	carboxyl (ketone) C=O	10	1771.63	0.21	aryl esters
	11	1768.06	0.39	aryl esters	11			

After the $ScCO_2$ treatment, the alkyl ether content in Coal #4 decreases slightly (1.06 %) while that in Coals #2-#4 increases (Table 8). As the coal rank increases, the increases become more pronounced. The contents of 2°C-O phenols, ethers, carboxyl (ketone) C=O, and aryl esters decrease significantly in the coal samples (Table 8), while the changes in the contents of 2°C-O sec. alcohols, 2°C-O aryl ethers, and carboxyl (quinone) C=O are complex. The 2°C-O sec. alcohol contents increase significantly in Coals #1 and #3 (by up to 297.65 % in Coal #3) but decrease in Coals #2 and #4 (1.75 % and 3.90 %, respectively; Table 8). The 2°C-O in aryl ether contents

increase in Coals #1 and #4 but decrease significantly in Coals #2 and #3 (Table 8). The carboxyl (quinone) C=O contents in Coal #3 decrease slightly (6.70 %) and increase in Coals #1, #2 and #4. The increase in the carboxyl (quinone) C=O content in Coals #1, #2 and #4 becomes more pronounced as the coal rank increases (Table 8). In general, the contents of oxygen-containing groups increase slightly in Coal #1 (13.65 %) due to oxidation reactions (Table 6) but decrease in Coals #2-#4 (Table 6) due to swelling (including hydrolysis reactions and nucleophilic addition reactions [8, 21]).

Table 9 Aliphatic C-H stretching bands extracted from the FTIR spectra.

Sample	Untreated				$ScCO_2$ treated			
	Peak index	Position, cm^{-1}	Area percentage, %	Assignment	Peak index	Position, cm^{-1}	Area percentage, %	Assignment
#1	1	2839.47	17.21	sym. R_2CH_2	1	2831.84	11.07	sym. R_2CH_2
	2	2859.57	20.12	sym. R_2CH_2	2	2856.01	24.08	sym. R_2CH_2
	3	2892.49	18.62	-R_3CH	3	2888.55	19.17	-R_3CH
	4	2920.20	32.39	asym. R_2CH_2	4	2919.25	33.74	asym. R_2CH_2
	5	2952.43	11.65	asym. RCH_3	5	2953.79	11.94	asym. RCH_3
#2	1	2832.20	14.11	sym. R_2CH_2	1	2829.23	13.53	sym. R_2CH_2
	2	2858.87	23.32	sym. R_2CH_2	2	2857.70	24.19	sym. R_2CH_2
	3	2888.01	16.49	-R_3CH	3	2888.23	16.53	-R_3CH
	4	2915.12	32.51	asym. R_2CH_2	4	2915.96	33.01	asym. R_2CH_2
	5	2950.89	13.57	asym. RCH_3	5	2949.73	12.74	asym. RCH_3
#3	1	2826.24	16.47	sym. R_2CH_2	1	2828.28	9.66	sym. R_2CH_2
	2	2850.19	22.13	sym. R_2CH_2	2	2855.79	28.00	sym. R_2CH_2
	3	2872.46	12.20	sym. R_2CH_2	3	2884.33	10.59	-R_3CH
	4	2905.67	39.29	asym. R_2CH_2	4	2914.36	43.89	asym. R_2CH_2
	5	2951.97	9.91	asym. RCH_3	5	2954.21	7.86	asym. RCH_3
#4	1	2821.42	26.32	sym. R_2CH_2	1	2826.68	8.53	sym. R_2CH_2
	2	2844.44	27.26	sym. R_2CH_2	2	2851.65	22.18	sym. R_2CH_2
	3	2884.51	4.50	-R_3CH	3	2886.09	22.27	-R_3CH
	4	2913.17	9.84	asym. R_2CH_2	4	2918.57	34.64	asym. R_2CH_2
	5	2944.16	11.90	asym. R_2CH_2	5	2956.43	12.39	asym. RCH_3
	6	2957.46	20.18	asym. RCH_3	6	2826.68	8.53	sym. R_2CH_2

Note: sym. denotes symmetric; asym. denotes asymmetric.

3.3.3 Variations in $ScCO_2$ on aliphatic structures

The coal samples display 2 main absorption bands (peaks) at 2847-2858 cm^{-1} and 2918-2935 cm^{-1} that correspond to symmetrical (sym.) R_2CH_2 and asymmetrical (asym.) R_2CH_2 (Table 9). Therefore, the coal samples are dominated by -CH_2 and present low contents of -CH_3 (asym. RCH_3) and -CH (-R_3CH), indicating that the

aliphatic hydrocarbons in the coal samples are mainly unbranched structures and alicyclic structures with relatively few branches. As the coal rank increases, the aliphatic hydrocarbons in the coal gradually fall off, resulting in a significant decrease in the aliphatic hydrocarbon contents and I_1 and I_4 values. The aliphatic hydrocarbon contents in Coal #4 are only 0.93 % (Table 6, 7).

After the $ScCO_2$ treatment, the sym. R_2CH_2 content is basically unchanged in Coal #2 (only 0.78 %) and decreases in Coals #1, #3, and #4 (Table 9). The decrease in the sym. R_2CH_2 content in Coal #4 reaches 42.69 % (Table 9). The asym. R_2CH_2 contents in the coal samples increase and show an increasing trend as the coal rank increases, and the values in Coals #1, #2, #3, and #4 are 4.15 %, 1.55 %, 11.71 %, and 59.32 %, respectively (Table 9). The -R_3CH contents in the coal samples mainly decrease, whereas the asym. RCH_3 contents mainly increase (Table 9). Coal #4 displays the largest increase in the -R_3CH content (395.03 %) and a decrease in the asym. RCH_3 content (38.61 %; Table 9). In general, the aliphatic hydrocarbon contents (including -CH_2, -CH_3, and -CH) display a decreasing trend in Coals #1 and #3 and increase slightly in Coals #2 and #3 due to the large increase in asym. RCH_3 and asym. R_2CH_2 contents (Table 6). However, the I_1 value of Coal #2 increases slightly, whereas the I_1 values of Coals #1, #3, and #4 decrease (Table 7). The asym. RCH_3 contents generally decrease, indicating that the branches of the aliphatic hydrocarbon chains have low bond dissociation energies that give priority to bond dissociation reactions. These reactions are the main reason for the decrease in the aliphatic hydrocarbon contents of Coals #1 and #3. The I_4 values of the coal samples increase, which is consistent with the increase in the asym. R_2CH_2 contents (Table 7). As the coal rank increases, the I_4 values significantly increase (Table 7), indicating that the aliphatic hydrocarbon chains are dominated by polyaddition reactions. The polyaddition reactions are stronger in the high-rank coals, resulting in an increase in the aliphatic hydrocarbon chain length.

3.3.4 Variations in $ScCO_2$ on hydroxyl structures

Five types of hydroxyl groups are observed in the coal samples: OH-N, ring hydroxyls, OH-O, OH-OH, OH-π, and ·OH (Table 10). The coal samples are dominated by OH-OH and OH-O and display low contents of other hydroxyl groups (Table 10). Similar to the oxygen-containing groups, the hydroxyl group contents decrease significantly as the coal rank increases (Table 6).

After the $ScCO_2$ treatment, the OH-N contents in the coal samples increase while the contents of ring hydroxyls, OH-O, OH-OH, OH-π, and ·OH are more complex (Table 10). The ring hydroxyl content in Coal #3 decreases significantly, whereas that in Coal #1, #2, and #4 increases significantly (26.59-179.50 %; Table 10). The OH-π

contents in Coals #1 and #4 decrease significantly (16.66 % and 17.52 %, respectively), while those in #2 and #3 increase significantly (29.11 % and 95.90 %, respectively; Table 10). The content of OH in Coal #1 decreases significantly (125.38 %), whereas such content was not observed in Coal #3 (Table 10). The contents of ring hydroxyls, OH-π, and ·OH in the coal samples are low, and these species make small contributions to the changes in the hydroxyl group contents, which are determined by OH-OH and OH-O. The OH-OH and OH-O contents in Coal #1 decrease significantly (18.72 % and 11.96 %, respectively), resulting in a significant decrease in the hydroxyl group contents (Table 10). In Coal #2, the OH-OH content decreases slightly (2.48 %) while the OH-O content increases significantly (18.53 %); thus, the hydroxyl group content increases significantly (Table 10). The OH-OH and OH-O contents in Coals #3 and #4 increase, especially in Coal #3, which presents an increase in OH-OH contents of 278.13 %, and an increase in the hydroxyl group contents is observed in Coals #3 and #4 (Table 10). Therefore, the hydroxyl groups in Coal #1 give priority to oxidation reactions, resulting in a decrease in the hydroxyl group contents. In Coals #2-#4, however, the hydroxyl groups are dominated by swelling, resulting in an increase in the hydroxyl group contents (Table 6). Due to the significant changes in and large contents of the hydroxyl groups, the I_3 value is determined by the hydroxyl groups to a larger extent, especially the increase observed in the I_3 values of Coals #2 and #3 (Table 7).

Table 10 Hydroxyl functional groups extracted from the FTIR spectra.

Sample	Untreated				$ScCO_2$ treated			
	Peak index	Position, cm^{-1}	Area percentage, %	Assignment	Peak index	Position, cm^{-1}	Area percentage, %	Assignment
#1	1	3056.23	0.63	OH-N	1	3053.16	0.66	OH-N
	2	3122.35	1.15	OH-N	2	3135.19	1.74	OH-N
	3	3175.82	2.31	OH-N	3	3189.15	3.62	ring hydroxyl
	4	3223.47	4.58	ring hydroxyl	4	3240.43	5.85	ring hydroxyl
	5	3279.87	9.10	OH-O	5	3289.37	7.17	OH-O
	6	3330.76	8.39	OH-O	6	3332.16	8.01	OH-O
	7	3375.37	15.31	OH-O	7	3371.81	11.48	OH-O
	8	3421.15	21.76	OH-OH	8	3411.31	19.44	OH-OH
	9	3467.69	16.15	OH-OH	9	3457.94	13.94	OH-OH
	10	3501.60	6.09	OH-π	10	3500.91	11.53	OH-π
	11	3529.11	7.05	OH-π	11	3541.40	9.32	OH-π
	12	3551.53	3.23	OH-π	12	3572.10	3.77	OH-π
	13	3571.30	2.70	OH-π	13	3597.52	3.48	·OH
	14	3590.99	1.54	·OH	14			
#2	1	3070.43	1.34	OH-N	1	3068.42	0.59	OH-N
	2	3103.74	0.36	OH-N	2	3102.11	0.39	OH-N

	3	3166.95	0.48	OH-N	3	3171.67	0.28	OH-N
	4	3202.30	0.39	ring hydroxyl	4	3208.92	1.09	ring hydroxyl
	5	3261.77	1.67	OH-O	5	3262.68	4.07	OH-O
	6	3337.81	7.71	OH-O	6	3323.22	8.34	OH-O
	7	3381.10	19.72	OH-O	7	3377.08	22.07	OH-O
	8	3424.96	29.44	OH-OH	8	3425.72	24.01	OH-OH
	9	3463.77	14.44	OH-OH	9	3472.08	18.78	OH-OH
	10	3506.23	16.55	OH-π	10	3519.35	13.01	OH-π
	11	3551.92	7.91	OH-π	11	3569.36	7.38	OH-π
	1	3112.68	1.54	OH-N	1	3064.89	0.31	OH-N
	2	3168.42	6.57	OH-N	2	3100.87	0.11	OH-N
	3	3211.23	4.47	ring hydroxyl	3	3169.55	0.51	OH-N
	4	3273.15	6.76	OH-O	4	3214.68	1.95	ring hydroxyl
	5	3318.04	13.10	OH-O	5	3271.17	6.23	OH-O
#3	6	3379.48	7.46	OH-O	6	3323.10	7.42	OH-O
	7	3443.50	6.05	OH-OH	7	3371.30	16.57	OH-O
	8	3493.96	6.12	OH-OH	8	3422.43	29.26	OH-OH
	9	3535.15	0.51	OH-π	9	3472.34	16.76	OH-OH
	10	3555.18	10.15	OH-π	10	3521.32	13.09	OH-π
	11	3592.93	37.27	·OH	11	3573.79	7.80	OH-π
	1	3054.17	1.27	OH-N	1	3082.43	0.14	OH-N
	2	3123.53	0.25	OH-N	2	3130.15	0.33	OH-N
	3	3167.43	0.46	OH-N	3	3176.63	0.86	OH-N
	4	3215.03	1.82	ring hydroxyl	4	3219.48	2.31	ring hydroxyl
	5	3264.64	5.62	OH-O	5	3272.46	6.48	OH-O
#4	6	3319.29	9.55	OH-O	6	3325.77	9.60	OH-O
	7	3371.57	15.39	OH-O	7	3374.59	16.74	OH-O
	8	3424.68	26.04	OH-OH	8	3426.24	27.47	OH-OH
	9	3474.56	15.67	OH-OH	9	3477.74	16.33	OH-OH
	10	3525.28	16.34	OH-π	10	3527.59	13.24	OH-π
	11	3576.90	7.59	OH-π	11	3577.51	6.50	OH-π

4. Discussion

4.1 Error analyses

(1) Sample preparation

Coal has great heterogeneity in its lithotypes, macerals, organic groups, and pore structure. The coal samples used in the CO_2 adsorption test, FTIR, and XRD cannot be reacted with $scCO_2$ and H_2O and thus could not be used for the CO_2 adsorption test, FTIR, and XRD because they may lead to errors in the results of the pore size distribution and macromolecular structure of the coal samples. To minimize this error, 4-5 kg coal with the same

lithotypes and macerals were selected for each coal sample, which are clarains selected from a bright coal layer; this process is similar to that used in our previous paper [12]. Then, the samples were crushed and sieved into different grain sizes to ensure similar characteristics.

(2) Experimental method

Although micropores are difficult to capture completely, small angle X-ray scattering (SAXS) and small angle neutron scattering (SANS) are able to characterize micropores [38]. However, SAXS and SANS are not commonly available [38], and the CO_2 adsorption test is still the most commonly used and effective method of characterizing the micropore structure, although this method only covers micropores ranging from 0.30 to 1.50 nm in the coal samples.

Since the pore size distribution determined by the CO_2 adsorption test was used for the model fitting analysis, fitting errors are inevitable. In this study, the pore size distribution is estimated via DFT analysis, which is the most accepted analysis method for micropores. The calculation accuracy of the DFT analysis is determined largely by the geometry model of the pores assumed in the model, e.g., cylindrical pores, spherical pores, and slit-shaped pores. To minimize this error, a slit-shaped pore model was chosen to describe the micropores in coal because this model is generally accepted by scholars for pore size distribution analyses in coal. Therefore, the influence of the analysis method on the pore size distribution can be ignored.

4.2 Effects of chemical structures on micropores

Changes in the chemical structure of coal, including changes in the aromatic layers of crystallites and among the crystallites, can lead to changes in the volume and size distribution of micropores.

4.2.1 Effects of crystallites on micropores

The changes in the peak values distributed at 0.32 nm and 0.42 nm are consistent with the changes in d_{002}. The d_{002} values of the bituminous coal increase slightly, while the peaks located at 0.32 nm and 0.42 nm increase slightly. For example, after the $ScCO_2$ treatment, the high-volatile bituminous coal displays one additional small peak located at 0.36 nm. The d_{002} values of the semi-anthracite and anthracite coal decrease, while the peaks that occur at 0.32 nm and 0.42 nm disappear. Furthermore, the changes in the d_{002} values are consistent with the changes in the volume of micropores with widths <0.46 nm, and these quantities display a positive correlation (Fig. 5a). In conclusion, micropores with widths <0.46 nm are mainly provided by the inter-layer spacing of the aromatic layers and the changes in d_{002} after the $ScCO_2$ treatment determine the volume of micropores with widths <0.46 nm.

The heterocycles and non-condensed polynuclear aromatic compounds in the aromatic structure of bituminous coal have weak bond energy and are easily detached by the swelling caused by $ScCO_2$. The falling off of heterocycles and non-condensed polynuclear aromatic compounds causes the rearrangement of the aromatic layers and loosens the internal structure of the aromatic crystallites in coal, and it finally increases the d_{002} values, which is the main reason for the increase in the volume of micropores with widths <0.46 nm in the bituminous coal.

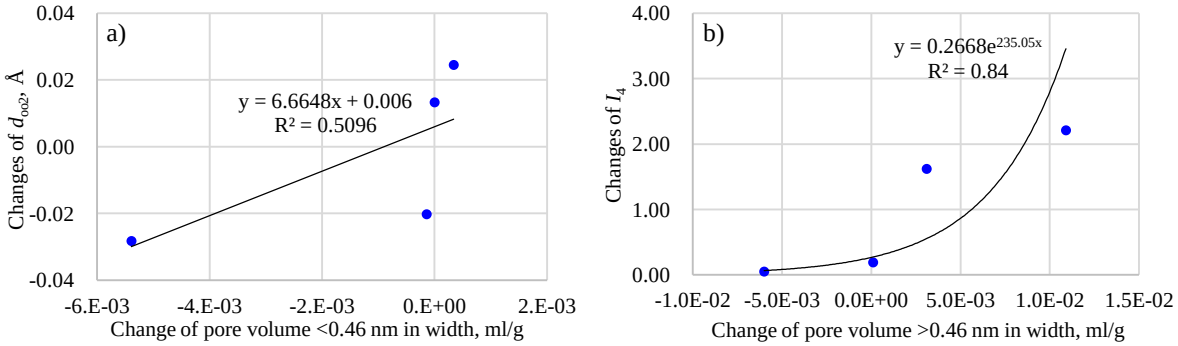

Fig. 5 Relationships between the changes in micropore volume and the d_{002} and I_4 values of the coal samples

Small amounts of the aromatic layers in the semi-anthracite and anthracite coal are connected by cross-links with low bond energies, e.g., $-CH_2-CH_2-$, $-CH_2-O-$, and -O-. The breaking of these cross-links caused by swelling results in the destruction and falling off of the aromatic layers. Compared with bituminous coal, the large amounts of residual aromatic layers are crosslinked with carbon-carbon bonds (C_{Ar}-C_{Ar}), and their arrangement is more regular and compact, resulting in small d_{002} values. In addition, the falling off of cross-links with low bond energies promotes the formation of C_{Ar}-C_{Ar} between the aromatic layers through polyaddition reactions, resulting in a decrease in d_{002}. Taken together, the falling off of cross-links with low bond energies and the formation of C_{Ar}-C_{Ar} cross-links between the aromatic layers cause the internal structure of the aromatic crystallites in the semi-anthracite and anthracite coal to become more regular and compact. This process is the main reason for the observed decrease in the volume of micropores with widths <0.46 nm in the semi-anthracite and anthracite coal after the $ScCO_2$ treatment.

4.2.2 Effects of macromolecules on micropores

Micropores with widths >0.46 nm are pores in the macromolecular structure of coal, and when they are formed by the directional arrangement of aromatic crystallites, they are known as intermolecular pores. The volumes of these pores are determined by the macromolecular structure of coal and influenced by the arrangement of aromatic crystallites, aliphatic hydrocarbon chain lengths, and low molecular compound contents. Therefore, the changes in the peaks located at 0.50 nm, 0.62 nm, 0.75 nm, and 0.82 nm are consistent with the changes in the arrangement

of aromatic crystallites, the aliphatic hydrocarbon chain lengths, and the low molecular compound contents (Fig. 5b).

The directional arrangement of aromatic crystallites may decrease the width and volume of the micropores by squeezing the pores between the aromatic crystallites and making the macromolecular structure of the coal more uniform [15]. Bituminous coal has a low condensation degree of aromatic crystallites, and under acidic conditions, its aliphatic hydrocarbon branches and oxygen-containing groups can easily be broken to generate free radicals and fallen off via the bond dissociation reaction of the alkyl groups and swelling, thereby resulting in the breaking of aliphatic hydrocarbon chains. The broken aliphatic hydrocarbon chains connected to the aromatic rings are likely to form new aliphatic hydrocarbon chains and aromatic compounds via addition reactions and polyaddition reactions, resulting in an increase in the directional arrangement of the aromatic crystallites, which can be improved by an increase in the I_2, aromaticity (AR2), f_a, and condensation degree (DOC2) of the bituminous coal (Table 7).

Similar to bituminous coal, the aliphatic hydrocarbon branches and oxygen-containing groups in the high-rank coal easily break away and fall off through bond dissociation reactions and swelling caused by $ScCO_2$. Compared with bituminous coal, the broken aliphatic hydrocarbon chains can easily capture the alkyl groups generated by the breaking of the low molecular compounds and cross-links, thereby increasing the aliphatic hydrocarbon chain length and the aliphatic hydrocarbon contents through polyaddition reactions. The formation of new aliphatic hydrocarbon chains in the high-rank coal loosen the macromolecular structure of coal and decrease the directional arrangement of aromatic crystallites, which can be improved by a decrease in I_2, AR2, f_a, and DOC2 (Table 7).

The increase in the length of the aliphatic hydrocarbon chain-connected aromatic crystallites leads to the loosening of the macromolecular structure of coal. This process is the main reason for the increase in the width and volume of the micropores, whereas the dissolution of aliphatic hydrocarbon branches and low molecular compounds promotes the generation of micropores and increases the width and volume of the micropores. However, these processes differ significantly in terms of their effects on coals of different ranks. As the coal rank increases, the aliphatic hydrocarbon chain length increases exponentially due to $ScCO_2$ (Fig. 5b). The change in the aliphatic hydrocarbon chain length varies from a slight increase for high-volatile bituminous coal (1.80 %), a modest increase for low-volatile bituminous coal (7.92 %), a large increase for semi-anthracite coal (40.81 %) and a significant increase for anthracite coal (374.58 %). This result shows that the influence of $ScCO_2$ on the aliphatic hydrocarbon chain length is weak in the bituminous coal and is more significant in the anthracite coal.

In conclusion, the changes in the width and volume of micropores with widths >0.46 nm in coal are caused by the directional arrangement of aromatic crystallites and an increase in the aliphatic hydrocarbon chain lengths. The decrease in the micropore width and volume in the high-volatile bituminous coal caused by the directional arrangement of aromatic crystallites dominates the increase in micropore width and volume caused by the increase in the aliphatic hydrocarbon chain length, resulting in the observed decrease in micropore width and volume in the high-volatile bituminous coal. Furthermore, the directional arrangement of aromatic crystallites has a weak influence on the pore size distribution. The influence of the directional arrangement of aromatic crystallites on the width and volume of the micropores in the low-volatile bituminous coal decreases and the influence of the aliphatic hydrocarbon chain length on micropore width and volume increases significantly. These changes result in an increasing trend in micropore width under the peaks located at 0.50 nm and 0.62 nm and no apparent change in the micropore volume. The increases in the width and volume of micropores in the high-rank coal caused by the increase in the aliphatic hydrocarbon chain length is dominant, and the decrease in the directional arrangement of aromatic crystallites increases the width and volume of the micropores, resulting in an increase in the width and volume of micropores with widths >0.46 nm. In addition, the increase in the aliphatic hydrocarbon chain length in the anthracite coal is much larger than that of the semi-anthracite coal, and the increases in the width and volume of the micropores in the anthracite coal are more evident, resulting in a greater increase in the width and volume of the micropores in the anthracite coal.

5. Conclusions

In this paper, the changes in the micropore structure, chemical structure, and organic groups noted in four samples of coal with different ranks observed after $ScCO_2$-H_2O treatment and their mechanisms are discussed. The following conclusions can be drawn from this study.

(1) After the $ScCO_2$ treatment, the volume of the micropores with widths <0.46 nm in the high-volatile bituminous coal increases slightly. As the coal rank increases, the decrease in the volume of micropores with widths <0.46 nm in the low-volatile bituminous, semi-anthracite, and anthracite coal becomes more pronounced. Micropores with widths <0.46 nm are mainly produced by the inter-layer spacing of the aromatic layers. Swelling caused by $ScCO_2$ detach heterocycles and non-condensed polynuclear aromatics in the high-volatile bituminous coal and loosens the internal structure of the aromatic crystallites, resulting in a slight increase in the volume of micropores with widths <0.46 nm. This swelling breaks the cross-links with low bond energies in the semi-anthracite and anthracite coal, and polyaddition reactions form C_{Ar}-C_{Ar} cross-links between the aromatic

layers, causing the internal structure of the aromatic crystallites to become more regular and compact. This process is the main reason underlying the observed decrease in the volume of micropores with widths <0.46 nm.

(2) After the $ScCO_2$ treatment, the volume of micropores with widths >0.46 nm in the high-volatile bituminous coal decrease, whereas these volume in the low-volatile bituminous, semi-anthracite, and anthracite coal increase. Micropores with a width >0.46 nm are pores in the macromolecular structure of coal formed by the directional arrangement of aromatic crystallites, and their volumes are determined by the arrangement of aromatic crystallites and the aliphatic hydrocarbon chain length. The breaking of bonds in the high-volatile bituminous coal caused by the falling off of aliphatic hydrocarbon branches and oxygen-containing groups forms new aliphatic hydrocarbon chains and aromatic compounds via addition and polyaddition reactions. These reactions increase the directional arrangement of aromatic crystallites, resulting in a decrease in the volume of micropores with widths >0.46 nm. As the coal rank increases, the aliphatic hydrocarbon chain length gives priority to the macromolecular structure of coal after the $ScCO_2$ treatment, resulting in an increase in the volume of micropores with widths >0.46 nm in semi-anthracite and anthracite coal.

Acknowledgements

This study was supported by the National Natural Science Foundation of China (Nos. 41330638, 41727801, and 41402135), the National Key Research and Development Plan (No. 2018YFB0605601), the National Key Technologies R&D Program (No. 2016YFE0102500), and the Natural Science Foundation of Jiangsu Province (No. BK20171188). We would like to thank the research students from the China University of Mining and Technology for their assistance in coal sampling and experimental work.

References

[1] Liu CJ, Wang GX, Sang SX, Rudolph V. Changes in pore structure of anthracite coal associated with CO_2 sequestration process. Fuel 2010; 89:2665-2672.

[2] Bergen FV, Tambach T, Pagnier H. The role of CO_2-enhanced coalbed methane production in the global CCS strategy. Energ Procedia 2011; 4:3112-3116.

[3] Rodosta T, Litynski J, Plasynski S, Spangler L, Finley R, Steadman E, Ball D, Hill G, Mcpherson B, Burton E, Vikara D. U.S. Depantment of Energy's regional carbon sequetration partnership initiative: update on validation and development phases. Energy Procedia 2011; 4:3457-3464.

[4] Massarotto P, Golding SD, Bae JS, Iyer R, Rudolph V. Changes in reservoir properties from injection of supercritical CO_2 into coal seams-A laboratory study. International Journal of Coal Geology 2010; 82:269-279.

[5] Day S, Duffy G, Sakurovs R, Weir S. Effect of coal properties on CO_2 sorption capacity under supercritical conditions.

International Journal of Greenhouse Gas Control 2008; 2:342-352.

[6] Kiyama T, Nishimoto S, Fujioka M, Xue ZQ, Ishijima Y, Pan ZJ, Connell LD. Coal swelling strain and permeability change with injecting liquid/supercritical CO_2 and N_2 at stress-constrained conditions. International Journal of Coal Geology 2011; 85:56-64.

[7] Mavhengere P, Maphala T, Wagner N. Physical and structural effects of carbon dioxide storage on vitrinite-rich coal particles under subcritical and supercritical conditions. International Journal of Coal Geology 2015; 150:1-6.

[8] Dawson GKW, Golding SD, Biddle D, Massarotto P. Mobilisation of elements from coal due to batch reactor experiments with CO_2 and water at 40 ºC and 9.5 MPa. International Journal of Coal Geology 2015; 140:63-70.

[9] Liu SQ, Sang SX, Liu HH, Zhu QP. Growth characteristics and genetic types of pores and fractures in a high-rank coal reservoir of the southern Qinshui basin. Ore Geology Reviews 2015; 64:140-15.

[10] Wang KR, Xu TF, Wang FG, Tian HL. Experimental study of CO_2-brine-rock interaction during CO_2 sequestration in deep coal seams. International Journal of Coal Geology 2016; 154-155:265-274.

[11] Wang Q, Ye JB, Yang HY, Liu Q. Chemical composition and structural characteristics of oil shales and their kerogens using Fourier Transform Infrared (FTIR) Spectroscopy and Solid-State ^{13}C Nuclear Magnetic Resonance (NMR). Energy & Fuels 2016; 30:6271-6280.

[12] Liu SQ, Ma JS, Sang SX, Wang T, Du Y, Fang HH. The effects of supercritical CO_2 on mesopore and macropore structure in bituminous and anthracite coal. Fuel 2018; 223:32-43.

[13] Kolak JJ, Burruss RC. Geochemical investigation of the potential for mobilizing non-methane hydrocarbons during carbon dioxide storage in deep coal beds. Energy & Fuels 2006; 20:566-574.

[14] Mazumder S, van Hemert P, Busch A, Wolf K AA, Tejera-Cuesta P. Flue gas and pure CO_2 sorption properties of coal: A comparative study. International Journal of Coal Geology 2006; 67:267-279.

[15] Zhang KZ, Cheng YP, Li W, Wu DM, Liu ZD. Influence of supercritical CO_2 on pore structure and functional groups of coal: Implications for CO_2 sequestration. Journal of Natural Gas Science and Engineering 2017; 40:288-298.

[16] Pasquali I, Comi L, Pucciarelli F, Bettini R. Swelling, melting point reduction and solubility of PEG 1500 in supercritical CO_2. International Journal of Pharmaceutics 2008; 356:76-81.

[17] Jonathan JK, Paul CH, Leslie FR, Warwick PD, Burruss RC. Using ground and intact coal samples to evaluate hydrocarbon fate during supercritical CO_2 injection into coal beds effects of particle size and coal moisture. Energy & Fuels 2015; 29:5187-5203.

[18] Stahl E, Schilz W, Schütz E. A quick method for the microanalytical evaluation of the dissolving power of supercritical gases. Angewandte Chemie International Edition in English 1978; 17:731-738.

[19] Mirzaeian M, Hall PJ. The interactions of coal with CO_2 and its effects on coal structure. Energy & Fuels 2006; 20:2022-2027.

[20] Mirzaeian M, Hall PJ, Jirandehi HF. Study of structural change in Wyodak coal in high-pressure CO_2 by small angle neutron scattering. Journal of Materials Science 2010; 45:5271-5281.

[21] Gathitu BB, Chen W, Michael M. Effect of coal interaction with supercritical CO_2 Physical structure. Industrial & Engineering Chemistry Research 2009; 10:5024-5034.

[22] Okolo GN, Everson RC, Neomagus HWJP, Roberts MJ, Sakurovs R. Comparing the porosity and surface areas of coal as

565 measured by gas adsorption, mercury intrusion and SAXS techniques. Fuel 2015; 141:293-304.
566 [23] Liu CJ, Wang GX, Sang SX, Gilani W, Rudolph V. Fractal analysis in pore structure of coal under conditions of CO_2
567 sequestration process. Fuel 2015; 139:125-132.
568 [24] Liu SQ, Sang SX, Wang G, Ma JS, Wang X, Wang WF, Du Y, Wang T. FIB-SEM and X-ray CT characterization of
569 interconnected pores in high-rank coal formed from regional metamorphism. Journal of Petroleum Science and Engineering 2017;
570 148:21-31.
571 [25] Clarkson CR, Bustin MR. Variation in micropore capacity and size distribution with composition in bituminous coal of the
572 Western Canadian Sedimentary Basin: Implications for coalbed methane potential. Fuel 1996; 75:1483-1498.
573 [26] Bustin RM, Clarkson CR. Geological controls on coalbed methane reservoir capacity and gas content. International Journal of
574 Coal Geology 1998; 38:3-26.
575 [27] André L, Audigane P, Azaroual M, Menjoz A. Numerical modeling of fluid-rock chemical interactions at the supercritical
576 CO_2-liquid interface during CO_2 injection into a carbonate reservoir, the Dogger aquifer (Paris Basin, France). Energy Conversion
577 and Management 2007; 48:1782-1797.
578 [28] Dutka B, Kudasik M, Pokryszka Z, Skoczylasa N, Topolnickia J, Wierzbickia M. Balance of CO_2/CH_4 exchange sorption in a
579 coal briquette. Fuel Processing Technology 2013; 106:95-101.
580 [29] Dutka B, Kudasik M, Topolnicki J. Pore pressure changes accompanying exchange sorption of CO_2/CH_4 in a coal briquette. Fuel
581 Processing Technology 2012; 100:30-34.
582 [30] Hao SQ, Kim S, Qin Y. Enhanced CO_2 gas storage in coal. Industrial & Engineering Chemistry Research 2013 52:18492-18497.
583 [31] Mastalerz M, Drobniak A, Walker R, Morse D. Coal lithotypes before and after saturation with CO_2; insights from micro- and
584 mesoporosity, fluidity, and functional group distribution. International Journal of Coal Geology 2010; 83:467-474.
585 [32] Kutchko BG, Goodman AL, Rosenbaum E, Natesakhawat S, Wagner K. Characterization of coal before and after supercritical
586 CO_2 exposure via feature relocation using field-emission scanning electron microscopy. Fuel 2013; 107:777-786.
587 [33] Sonibare OO, Haeger T, Foley SF. Structural characterization of Nigerian coals by X-ray diffraction, Raman and FTIR
588 spectroscopy. Energy 2010; 35:5347-5353.
589 [34] Wang GX, Wei XR, Wang K, Massarotto P, Rudolph V. Sorption-induced swelling/shrinkage and permeability of coal under
590 stressed adsorption/desorption conditions. International Journal of Coal Geology 2010; 83:46-54.
591 [35] Pierotti RA, Rouquerol J. Reporting physisorption data for gas/solid systems with special reference to the determination of
592 surface area and porosity. Pure and Applied Chemistry 1985; 57:603-619.
593 [36] Jin K, Cheng YP, Liu QQ, Zhao W, Wang L, Wang F, Wu DM. Experimental investigation of pore structure damage in
594 pulverized coal: Implications for methane adsorption and diffusion characteristics. Energy & Fuels 2016; 30:10383-10395.
595 [37] Hou S, Wang X, Wang X, Yuan Y, Pan S, Wang X. Pore structure characterization of low volatile bituminous coals with different
596 particle size and tectonic deformation using low pressure gas adsorption. International Journal of Coal Geology 2017; 183:1-13.
597 [38] Zhao J, Xu H, Tang D, Mathews JP, Li S, Tao S. A comparative evaluation of coal specific surface area by CO_2 and N_2
598 adsorption and its influence on CH_4 adsorption capacity at different pore sizes. Fuel 2016; 183:420-431.

599 [39] Zhao J, Xu H, Tang D, Mathews JP, Li S, Tao S. Coal seam porosity and fracture heterogeneity of macrolithotypes in the
600 Hancheng Block, eastern margin, Ordos Basin, China. International Journal of Coal Geology 2016; 159:18-29.
601 [40] Chen Y, Mastalerz M, Schimmelmann A. Characterization of chemical functional groups in macerals across different coal ranks
602 via micro-FTIR spectroscopy. International Journal of Coal Geology 2012; 104:22-33.
603 [41] Craddock PR, Le Doan TV, Bake K, Polyakov M, Charsky AM, Pomerantz AE. Evolution of kerogen and bitumen during
604 thermal maturation via semi-open pyrolysis investigated by Infrared Spectroscopy. Energy & Fuels 2015; 29:2197-2210.
605 [42] Zhang XD, Zhang S, Li PP, Ding Z, Hao ZC. Investigation on solubility of multicomponents from semi-anthracite coal and its
606 effect on coal structure by Fourier transform infrared spectroscopy and X-ray diffraction. Fuel Processing Technology 2018;
607 174:123-131.
608 [43] Lu L, Sahajwalla V, Kong C, Harris D. Quantitative X-ray diffraction analysis and its application to various coals. Carbon 2001;
609 39:1821-1833.
610 [44] Machado ADS, Mexias AS, Vilela ACF, Osorio E. Study of coal, char and coke fines structures and their proportions in the
611 off-gas blast furnace samples by X-ray diffraction. Fuel 2013; 114:224-228.
612 [45] Ju YW, Jiang B, Hou QL, Wang GL. FTIR spectroscopic study on the stress effect of compositions of macromolecular structure
613 in tectonically deformed coals. Spectroscopy and Spectral Analysis 2005; 25:1216-1220.
614 [46] Iglesias MJ, del Río JC, Laggoun-Défarge F, Cuesta MJ, Suárez-Ruiz I. Control of the chemical structure of perhydrous coals;
615 FTIR and Py-GC/MS investigation. Journal of Analytical and Applied Pyrolysis 2002; 62:1-34.